REPORT DOCUMENTATION PAGE

Form Approved OMB NO. 0704-0188

1. REPORT DATE (DD-MM-YYYY)	2. REPORT TYPE	3. DATES COVERED (From - To)
06-04-2022	Final Report	15-Apr-2020 - 31-Dec-2021

4. TITLE AND SUBTITLE
Final Report: Experimental Investigation to Inform the Design and Development of a High-Speed Projectile

5a. CONTRACT NUMBER
W911NF-20-2-0076

5b. GRANT NUMBER

5c. PROGRAM ELEMENT NUMBER
111111

6. AUTHORS

5d. PROJECT NUMBER

5e. TASK NUMBER

5f. WORK UNIT NUMBER

7. PERFORMING ORGANIZATION NAMES AND ADDRESSES
Florida State University
Sponsored Research Administration
874 Traditions Way, Third Floor
Tallahassee, FL 32306 -4166

8. PERFORMING ORGANIZATION REPORT NUMBER

9. SPONSORING/MONITORING AGENCY NAME(S) AND ADDRESS (ES)
U.S. Army Research Office
P.O. Box 12211
Research Triangle Park, NC 27709-2211

10. SPONSOR/MONITOR'S ACRONYM(S)
ARO

11. SPONSOR/MONITOR'S REPORT NUMBER(S)
76819-EG.2

12. DISTRIBUTION AVAILIBILITY STATEMENT
Approved for public release; distribution is unlimited.

13. SUPPLEMENTARY NOTES
The views, opinions and/or findings contained in this report are those of the author(s) and should not contrued as an official Department of the Army position, policy or decision, unless so designated by other documentation.

14. ABSTRACT

15. SUBJECT TERMS

16. SECURITY CLASSIFICATION OF:			17. LIMITATION OF ABSTRACT	15. NUMBER OF PAGES	19a. NAME OF RESPONSIBLE PERSON
a. REPORT	b. ABSTRACT	c. THIS PAGE			Rajan Kumar
UU	UU	UU	UU		19b. TELEPHONE NUMBER 850-645-0149

RPPR Final Report
as of 07-Apr-2022

Agency Code: 21XD

Proposal Number: 76819EG **Agreement Number: W911NF-20-2-0076**
INVESTIGATOR(S):

Name: Ph.D. Mark Costello
Email: mark.costello@ae.gatech.edu
Phone Number: 4048943002
Principal: N

Name: Rajan Kumar
Email: rkumar@eng.famu.fsu.edu
Phone Number: 8506450149
Principal: Y

Organization: **Florida State University**
Address: Sponsored Research Administration, Tallahassee, FL 323064166
Country: USA
DUNS Number: 790877419 EIN: 591961248

Report Date: 31-Mar-2022 Date Received: 06-Apr-2022
Final Report for Period Beginning 15-Apr-2020 and Ending 31-Dec-2021
Title: Experimental Investigation to Inform the Design and Development of a High-Speed Projectile
Begin Performance Period: 15-Apr-2020 **End Performance Period:** 31-Dec-2021
Report Term: 0-Other

Submitted By: Rajan Kumar Email: rkumar@eng.famu.fsu.edu
Phone: (850) 645-0149

STEM Degrees: 0 **STEM Participants:** 2

Major Goals: The development of a high-speed weapon system requires detailed experimental and numerical investigations to better understand the complex flow-field involving three-dimensionality, crossflow separation, shock-boundary layer interactions, fluid-structure interactions, and unsteady wake-plume interactions. Theoretical and analytical methods such as DATCOM and MISL3 are often used as preliminary prediction tools, but those often fall short of detailed analysis due to their limited applicability and level of accuracy.

Over the last two decades, a large number of CFD tools based on both steady-state as well as time-accurate methods have been developed to obtain aerodynamic coefficients. Over the years the accuracy of these methods has been significantly improved, and their applicability is expanded to complex geometry. However, most of these CFD tools cannot accurately predict flows involving 3D crossflow separation, shock-boundary layer interactions, and fluid-structure interactions and therefore require further refinement based on experimental results. A detailed experimental investigation is therefore needed to validate high-fidelity simulation tools and understand fundamental flow physics for the development of precision projectiles.

The main objectives of this research were to generate a robust experimental database on the basic aerodynamic characteristics and the effectiveness of control surfaces at large deflections.

Accomplishments: An experimental study involving force and moment measurements, high-speed shadowgraphy, and surface oil flow visualization was conducted on a generic axisymmetric projectile configuration with low aspect-ratio fins at the Florida State University Polysonic Wind Tunnel. The main objectives of this study were to validate numerical simulations and generate an aerodynamic database for a range of Mach numbers (0.4 to 4) and control surface deflections.

Major Results: The results showed an excellent match between the experimental and numerical data for the baseline configuration. Surface oil flow visualization and shadowgraph images showed a few complex and interesting flow features such as body vortex and fin interactions, shock-shock, and shock-boundary layer interactions. Control surfaces were very effective for pitch and roll control at all Mach numbers and control deflections tested. Experimental results showed a significant variation in CN at higher angles of attack for Mach

numbers greater than Mach 2, as well as a significant reduction in roll orientation dependence. Significant variation between supersonic and transonic behavior was also observed when looking at control surface effectiveness. Overall, control surface effectiveness was notably reduced from Mach 0.7 to Mach 2, as well as changes in behavior with alpha were observed for both CPM and CRM. These observations, in conjunction with flow visualization, indicate there are significant compressibility effects on the shear layer produced by this configuration. While this would generally be expected, it is of interest to conduct a more detailed study into the underlying flow physics that causes these effects. The data collected here will be used as a basis for future studies with more advanced flow diagnostic techniques in the FSU PSWT to fully resolve and characterize the flow fields generated by this configuration across an extended Mach regime. The database generated will be very useful for further validation of the numerical tool and the design of control laws.

Training Opportunities: 1) Royce Pokela (Ph.D. student, FSU) participated as a graduate research assistant on this project. He was trained in the area of wind tunnel testing and flow diagnostics. In particular, he was trained to conduct high-speed shadowgraphy and force measurements using a six-component strain gauge balance.

2) Spenser Mickus (Ph.D. student, GT) also participated as a graduate research assistant on this project. He was trained in the area of aerodynamic modeling for flight dynamics and control.

Results Dissemination: Pokela, R., Kumar, R, and Vasile, J. D. (2021) “Experimental and Computational Aerodynamic Characterization of a Generic High-Speed Projectile Configuration”, AIAA AVIATION 2021 Forum, 2-6 August 2021, Virtual Event, AIAA 2021-2607 https://doi.org/10.2514/6.2021-2607.

Honors and Awards: Outstanding Research Accomplishment Award (2021) - Rajan Kumar, FAMU-FSU College of Engineering.

Protocol Activity Status:

Technology Transfer: Cooperative Research and Development Agreement (CRADA) between Army Research Lab and Florida State University ARL CRADA-17-031-J004
entitled “FLOW INTERACTION EFFECTS ON HIGH-SPEED WEAPON VEHICLE AERODYNAMICS".

PARTICIPANTS:

Participant Type: PD/PI
Participant: Rajan Kumar
Person Months Worked: 1.00 **Funding Support:**
Project Contribution:
National Academy Member: N

Participant Type: Co PD/PI
Participant: Mark Costello
Person Months Worked: 1.00 **Funding Support:**
Project Contribution:
National Academy Member: N

Participant Type: Graduate Student (research assistant)
Participant: Royce Pokela
Person Months Worked: 9.00 **Funding Support:**
Project Contribution:
National Academy Member: N

Participant Type: Graduate Student (research assistant)

RPPR Final Report
as of 07-Apr-2022

Participant: Spencer Mickus
Person Months Worked: 6.00 **Funding Support:**
Project Contribution:
National Academy Member: N

CONFERENCE PAPERS:

Publication Type: Conference Paper or Presentation **Publication Status:** 1-Published
Conference Name: AIAA AVIATION 2021 FORUM
Date Received: 12-Aug-2021 Conference Date: 06-Aug-2021 Date Published: 06-Aug-2021
Conference Location: VIRTUAL EVENT
Paper Title: Experimental and Computational Aerodynamic Characterization of a Generic High-Speed Projectile Configuration
Authors: Royce Pokela, Rajan Kumar, Joseph Vasile
Acknowledged Federal Support: **Y**

Partners

,

I certify that the information in the report is complete and accurate:
Signature: Rajan Kumar
Signature Date: 4/6/22 2:59PM

Experimental Investigation to Inform the Design and Development of a High-Speed Projectile

Royce Pokela* and Rajan Kumar†
Florida Center for Advanced Aero-Propulsion (FCAAP)
FAMU-FSU College of Engineering, Tallahassee, FL 32310

Joseph D Vasile‡
U.S. Army Combat Capabilities Development Command -
Army Research Laboratory, Aberdeen Proving Ground, MD 21005

Spencer Mickus § and Mark Costello¶
Georgia Institute of Technology, Atlanta, Georgia 30332

An experimental study involving force and moment measurements, high-speed shadowgraphy, and surface oil flow visualization was conducted on a generic axisymmetric projectile configuration with low aspect-ratio fins at the Florida State University Polysonic Wind Tunnel. The main objectives of this study were to validate numerical simulations and generate an aerodynamic database for a range of Mach numbers (0.4 to 4) and control surface deflections. Results showed an excellent match between the experimental and numerical data for the baseline configuration. Surface oil flow visualization and shadowgraph images showed a few complex and interesting flow features such as body vortex and fin interactions, shock-shock, and shock-boundary layer interactions. Control surfaces were very effective for pitch and roll control at all Mach numbers and control deflections tested. The database generated will be very useful for further validation of the numerical tool and the design of control laws.

I. Introduction

Development of high-speed projectiles and air vehicles requires detailed experimental and numerical investigations to build the aerodynamic database and advance the general understanding of complex flow-fields involving three-dimensionality, crossflow separation, shock-boundary layer interactions, fluid-structure interactions, unsteady wake-plume interactions, etc. Additionally, flow-fields experienced by an aerodynamic body vary significantly across an extended Mach range, particularly at transonic speeds involving non-linear effects. While there is a large selection of advanced computation tools specifically developed to assist in the design of high-speed projectiles, limitations still inhibit their ability to accurately model all complex flow phenomena. For that reason, experimental investigations continue to be used in conjunction with computational studies to provide validation data. In the present study, a series of wind tunnel tests and numerical simulations were conducted on an axisymmetric projectile configuration with very low aspect ratio fins.

Axisymmetric slender body aerodynamics has been studied extensively and the associated flow physics are generally well understood, showing that initial attached, vortex-free flow transitions to a separated symmetric vortex flow at low to moderate angles of attack ($\alpha > 5°$) and asymmetric vortex flow at high angles of attack ($\alpha > 25°$). Some of these studies were conducted for the purpose of validating both theoretical predictions and computational simulations [1–6], while others were conducted to better understand general flow physics [7–11]. Multiple recent studies on generic axisymmetric bodies were conducted at the Florida Center for Advanced Aero-Propulsion for both of these purposes, studying both general aerodynamic characteristics, high-alpha aerodynamics, control surface effectiveness, etc. Force measurements have been obtained from low speeds up to Mach 4 to characterize the basic aerodynamic characteristics of a generic axisymmetric slender body with tail fins, showing a notable variation in the onset of non-linearity of the

*Graduate Research Assistant, Department of Mechanical Engineering, AIAA Student Member
†Professor, Department of Mechanical Engineering, Associate Fellow AIAA
‡Aerospace Engineer, Weapons and Materials Research Directorate, FCDD-RLW-WD, AIAA Senior Member
§Graduate Research Assistant, Guggenheim School of Aerospace Engineering
¶William R.T. Oakes School Chair and Professor, Guggenheim School of Aerospace Engineering.

coefficient of normal force between subsonic, transonic, and supersonic flows. As expected, pitching moment and drag characteristics were strongly dependent on Mach number [12–14]. In a subsequent study, the effect of delta wings on the longitudinal aerodynamic characteristics was investigated [15].

From a flow physics perspective, it is known that additional aerodynamic surfaces increase the complexity of the flow-field with additional vortex flow introduced, amongst the other previously mentioned potential interactions as well. With this, comes significant interest in understanding the interaction of the shear layer with various fin configurations. This in part led to this study of a generic body with low-aspect ratio, high-chord length fins. Even at lower angles of attack, these type of fins can contribute heavily to the production of complex flow features and have potential effects on static stability, drag forces, and control surface effectiveness. Also, considering that fin generated normal force and roll angle orientation have been shown to have a relationship, even with small tail fins [16], the significance of this dependence for this configuration needed to be determined. Lastly, it was deemed important to determine how the magnitude of these effects varies from low speeds through highly compressible supersonic flow. A numerical investigation by Vasile and Sahu [17] to study the roll orientation-dependent aerodynamics of this model and obtain aerodynamic coefficients through both an inviscid solver and a Navier-Stokes viscous solver was conducted. The viscous effects were characterized and the resulting flow features were observed. The results showed that the roll orientation of the model had a notable effect on the longitudinal aerodynamic characteristics and the center of pressure location in part due to viscous forces on the fins. This was evident due to the disparity in resultant pitching moment values between the inviscid and viscous solvers [17]. In the present experimental study, force and moment measurements were carried out, along with flow visualization in the form of surface oil flow and high-speed shadowgraphy, to both validate and build upon those initial computational results. In addition, these general results will be used as a basis for more detailed and focused investigations into some of the flow phenomena observed.

Measurements were carried out over a range of Mach (0.4 - 4) and Reynolds numbers, angles of incidence and roll orientations. Flow features were observed in context of the acquired force and moment data to facilitate an understanding of the flow physics associated with this configuration. An excellent agreement between the experimental and computational data was observed, suggesting a further computational analysis to supplement understanding of the flow and to allow for a complete aerodynamic characterization of this configuration. Considering the generic features of this configuration, the results and analysis of the investigated flowfield can be applied to various future applications.

II. Experimental Setup and Test Techniques

A. Test Models

The experimental configuration in this study was a generic, axisymmetric cylinder body with four low aspect ratio fins. It featured a 3 diameter long, blunt von Kármán ogive nose with a 0.1 diameter blunt radius. The 0.83 inch diameter model had a slenderness ratio of 10. The root fin chord of thefins was 6 diameters long, and the fin span was approximately 1.6 inches. For this series of testing, two separate models were fabricated, including the baseline, fixed-fin model and a second model with detachable deflected control surfaces. Control surfaces had a chord of 16 mm and were hinged midchord at 8 mm. Detachable control surfaces were manufactured at 0°, ± 5°, 10°, and 20° to allow for positive and negative traditional elevator configurations and aileron roll configurations. Both models used the same physical nose, which included a 1 mm strip of silicon carbide particles, placed 1 diameter from the tip of the nose. This was done to artificially transition the boundary layer for simulation of a larger scale model. Drawings of each model are shown in figure 1. Screw holes were filled with repair putty that was dried and smoothed before testing. Additional information on this configuration can be obtained in Vasile et al. [18].

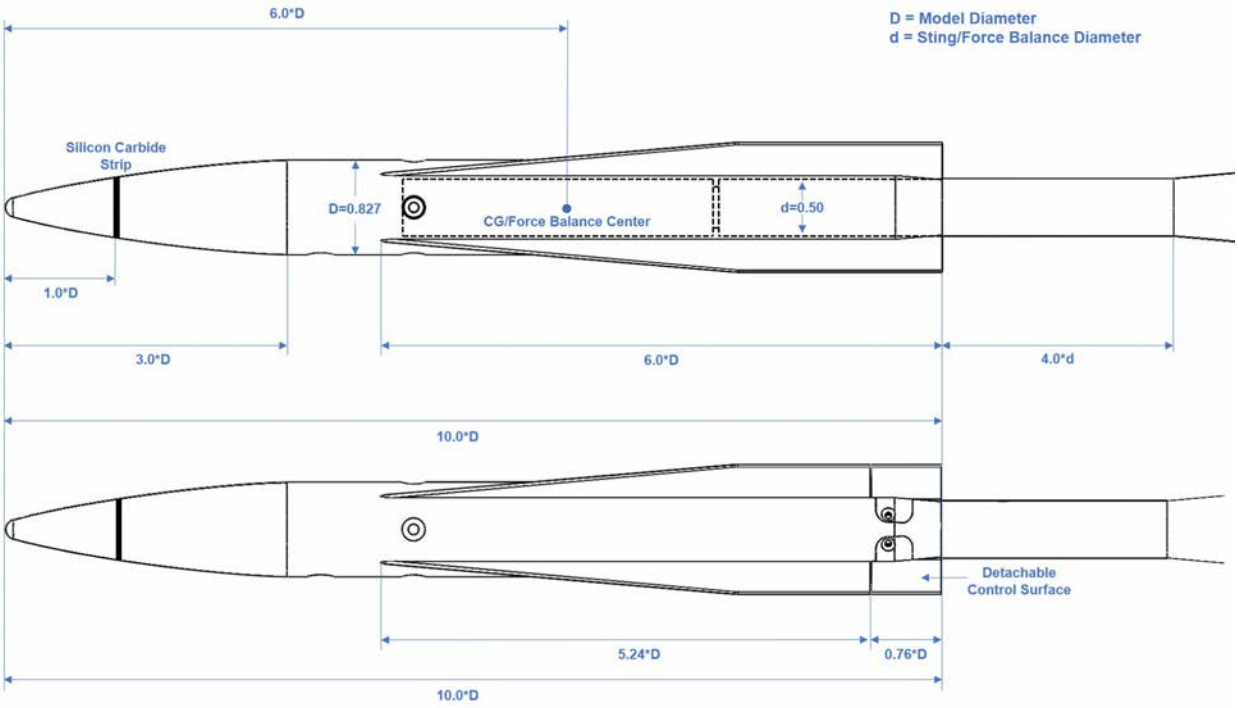

Fig. 1 Side drawing of each model tested in this series of experiments, shown at $\phi = 0°$.

B. Wind Tunnel Facility

The Florida State University Polysonic Wind Tunnel (PSWT) is a blowdown wind tunnel that operates in the subsonic, transonic, and supersonic regimes, up to Mach 5. Models can be sting, floor, or wall mounted within a 12" x 12" x 24" test section for subsonic and supersonic testing. For transonic testing, a separate 12" x 12" x 48" test section is used, which includes slotted walls to help accommodate transonic conditions. The rms pressure fluctuations at supersonic speeds, and turbulence intensity are less than 0.2 percent. Flow angularity in both pitch and yaw plane are less than 0.2 degrees.

Fig. 2 The Florida State University Polysonic Wind Tunnel (PSWT).

C. Measurement Techniques

1. Forces and Moments

Forces and moments were measured using a 0.5 inch diameter ARI MKXV, which is a 6-axis internal strain gage force balance. Maximum loads for normal force, side force, and axial force (at zero moments) were 200 lbs, 100 lbs, and 50 lbs, respectively. Maximum loads for pitching, yawing, and rolling moments (at zero forces) were 210 in.-lbs, 85 in.-lbs, and 50 in.-lbs, respectively. The selection of the force balance allowed for this model to be safely tested without overloading the balance on start up loads, while maintaining a desired level of sensitivity for quality results. The balance was sting mounted to a pitch and roll mechanism to acquire data during pitch and roll sweeps. Prior to the tests, the force balance was carefully calibrated. Additionally, prior to each individual run, the force balance underwent a "wind off" run where the upcoming pitch and roll sweep was conducted to obtain the forces and moments produced by the weight of the model and balance, to be removed from the test results in processing. Model base pressure was measured using two Kulite 30 psia unsteady pressure transducers to provide drag corrections that account for the presence of the sting. Each transducer was connected to tubing that was mounted on the sting at the rear of the model. Coefficients were then derived using the force balance data, base pressure measurements, and measured tunnel conditions. Sample equations for the coefficients are shown below.

$$CN = \frac{Normal\ Force}{q_\infty * S} \tag{1}$$

$$CPM = \frac{Pitching\ Moment}{q_\infty * S * D} \tag{2}$$

$$CA = \frac{Axial\ Force}{q_\infty * S} + CBP \tag{3}$$

$$CBP = \left(\frac{P_{base} - P_\infty}{q_\infty}\right)\left(\frac{D}{S}\right) \tag{4}$$

$$CD = (CN)sin(\alpha) + (CA)cos(\alpha) \tag{5}$$

The uncertainty of the force balance is ±0.1% of the full capacity for each element. The other two factors considered in the uncertainty for the derived coefficients (with the exception of axial force) are the dynamic pressure term, q_∞ and the measured model diameter, D, which was measured to ±0.001 inches (model diameter is included in the calculation of the cross-sectional area, S). The dynamic pressure term was ultimately derived from static and stagnation pressures measured in the wind tunnel. The derivation of the coefficient of axial force also included the base pressure measurements as shown in equations 3 and 4, where CBP is the base pressure correction term. Estimated maximum

uncertainty for each derived coefficient, calculated using the RSS method, was $\leq \pm 0.016$ and 0.011 for CN and CA, respectively. For moment coefficients, they are also $\leq \pm 0.016$ and $\leq \pm 0.011$ for CPM and CRM, respectively. Repeatability tests show that the measurement uncertainties are well within the estimated values.

2. Flow Visualization

High-speed shadowgraphy was acquired for each run that included force and moment measurements to help visualize flow features including shocks and trailing vortices. The shadowgraph setup utilized a Phantom camera, a high-speed LED circuit, and a delay generator. Each run was captured at 200 Hz. Post-processed images included here were captured directly from the produced cine files. Intensity rms analysis on 100 total frames per run was conducted to allow for increased definition of the flow features produced during the tests.

Surface oil flow visualization was obtained to capture and observe the development of surface flow features. The mixture used was made with fluorescent powder and mineral oil, which was illuminated with intense UV light. High-resolution video was obtained using a Prosilica GT camera and a long-pass light filter. The model was painted in a quadrant pattern with two separate colors to allow for the tracking of streaklines across the model. Oil flow visualization was conducted at $\alpha = 0°$ and $\alpha = 12°$ at Mach 0.7, 1.1, 2, and 4. At transonic conditions, the model was already pitched at the start of the test. At supersonic conditions, the model wasn't pitched until after the tunnel fully achieved conditions due to higher start up loads.

D. Numerical Simulations

The numerical study conducted here consisted of a custom aeromodel comprised of CFD++ RANS simulations, inviscid Cart3D simulations, and semi-empirical prediction using Missile Datcom. Coefficients from the 3D compressible RANS simulations were taken in a quasi-steady pitch sweep procedure at α=0°, 2°, 4°, 5°, and 10°, and at 22.5° roll increments. These results were further supplemented by the Cart3D and Missile DATCOM data to compute full pitch and roll sweeps. The ultra fine CFD++ mesh was created using Genesis Capstone. Additional details on the numerical simulations that were included in this aeromodel can be reviewed in [17, 19].

III. Results and Discussion

A. Normal Force Characteristics

1. Experimental Results

Initial coefficient of normal force and drag characteristics are shown for the baseline, fixed-fin configuration. The variation of CN with alpha is shown in figure 3 at subsonic, transonic, and supersonic speeds. The variation of CN with alpha is linear at low angles of incidence. At subsonic conditions, the difference in CN between Mach = 0.4 and Mach = 0.5 is minimal. It appears that flow separation is occurring as early as $\alpha = 4°$ as indicated by the onset of non-linearity. Initial separation is likely developing on the fin tips, as forebody separation typically develops between $5 - 12°$ for slender bodies. Further flow visualization will be needed to confirm this. At transonic conditions, flow behavior is similar to subsonic conditions from Mach = 0.6 through Mach 0.9. Very minor increases in CN with increased Mach number are observed near $\alpha = 12°$, but notable increases are not observed until Mach 1.1 and Mach 1.2. For low angles of attack ($\alpha < 4°$), maximum CN values are in the supersonic regime (Mach 2), but for angles of attack greater than 4°, CN generated by this configuration peaks at Mach 1.2. For the recently studied axisymmetric body with tail fins of similar slenderness ratio, this distinction was not observed, as CN values were higher at both Mach 1.1 and Mach 1.2 than at Mach 2 at all angles of attack measured (0°-12°), with overall maximum CN values occuring at Mach 1.2 [12]. For the present configuration, the difference in CN between all three Mach numbers in the supersonic regime is minimal until $\alpha > 4°$ where Mach 4 results diverge. Mach 2 and 3 results diverge past $\alpha > 6°$. The trend of change with Mach number is the opposite at supersonic conditions where there is a decrease in CN with increased Mach number at higher angles of attack. At higher alpha, Mach 4 results are the lowest of any Mach number. In the previous study [12], there was no significant decrease in CN with increased Mach number at all, potentially indicating that with this current configuration, the majority of the loss at Mach 4 is from the fins. The general normal force being produced by this configuration across Mach numbers is notably higher than that typically produced by slender bodies alone, but at Mach 4, CN begins to approach that produced by fin-less bodies.

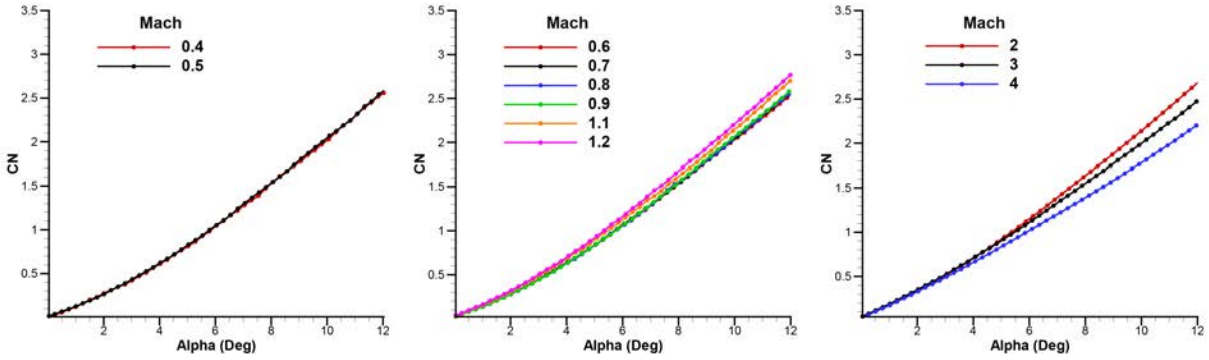

Fig. 3 Variation of coefficient of normal force with alpha at subsonic, transonic, and supersonic speeds, $\phi = 0°$.

The variation of CN with roll angle while at 12° angle of attack is shown in figure 4 to illustrate the roll angle dependence of the configuration and the overall influence of the fins. The results show the expected sinusoidal variation based on previous literature and the previous numerical study [16, 17], although only up to Mach 3. Maximum CN occurs with the model in the '+' configuration ($\phi = 45°$), while the minimum CN occurs with the model in the 'x' configuration ($\phi = 0°$). This dependence on roll angle is consistent throughout the entire subsonic and transonic regimes. However, the change in CN with roll angle decreases with an increase in Mach number above Mach 1.2 and is essentially non-existent at Mach 4.

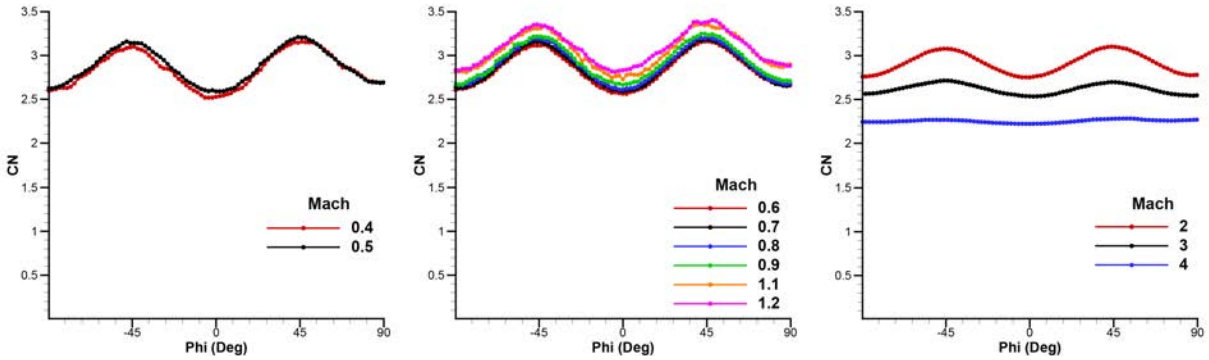

Fig. 4 Variation of coefficient of normal force with roll orientation at subsonic, transonic, and supersonic speeds, $\alpha = 12°$.

To better visualize the maximum change in CN with roll, as well as view how this difference varies with angle of attack, CN versus alpha curves are plotted together in both the '+' configuration and the 'x' configuration at Mach 0.7, 1.1, 2, and 4. At Mach 0.7, 1.1, and Mach 2, the roll angle dependence is in effect once the fins begin to produce lift, and the variation of CN clearly increases with increased alpha. The similarity in behavior at transonic speeds is apparent based on the minimal difference in CN at $\alpha = 6°$ and $\alpha = 12°$. At Mach 4 however, the overall lack of variation observed in figure 4 can be seen once again.

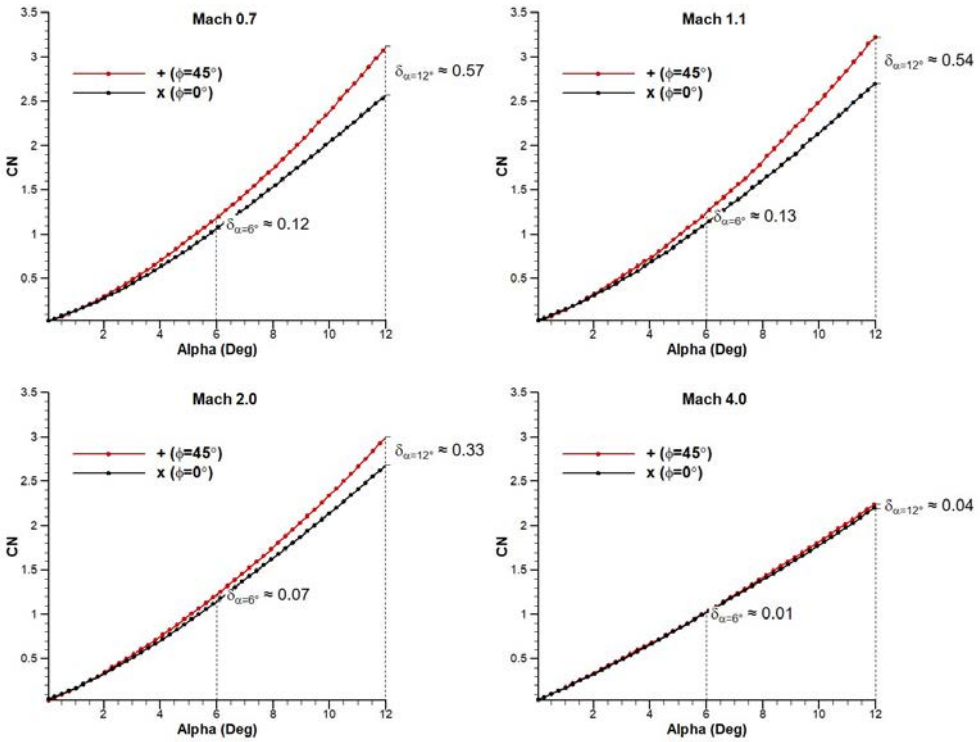

Fig. 5 Comparison of normal force characteristics at $\phi = 0°$ ('x' configuration) and $45°$ ('+' configuration).

This variation suggests that when the model is in the 'x' configuration, the vortices from the forebody are interacting with the leeward fins and causing a loss of lift, the potential for which has been mentioned previously [11, 16]. Presumably, this potential interaction is not occurring when the model is in the '+' configuration. It is also likely that in the 'x' configuration, the vortices from the windward fins are playing a role as well. Additionally, it is clear that the compressibility effects are significant beyond Mach 2. CN has shown to decrease above Mach 2 and it is likely that at these Mach 4 conditions, the normal force generated is highly dominated by the forebody, reducing the contribution of normal force that can even be lost by vortex-fin interactions. These effects will be of significant interest for the future study.

2. Comparison of Experimental and Numerical Results

Aerodynamic coefficients derived from the CFD simulations are compared to the experimental results for validation purposes. In this paper, the variation of CN with both angle of attack and roll angle are included to verify that the behavior previously discussed were also observed in numerical simulations. These comparisons are shown in figures 6 and 7. The CFD methods discussed here are outlined in section III. Data is presented once again at Mach 0.7, 1.1, 2, and 4 to include the behavior changes at higher Mach numbers.

Figure 6 shows the CFD results matching well with the experimental results at all four Mach numbers. The most consistent agreement shown here is at Mach 0.7. The CFD does underestimate CN at Mach 0.7 at both very low and high alpha, but not significantly. At Mach 1.1, 2, and 4, we see a difference in curve slope as the CFD curves change from slight underestimation at very low alpha, to slight overestimation at higher alpha. In general, the comparison between experimental and CFD results is excellent.

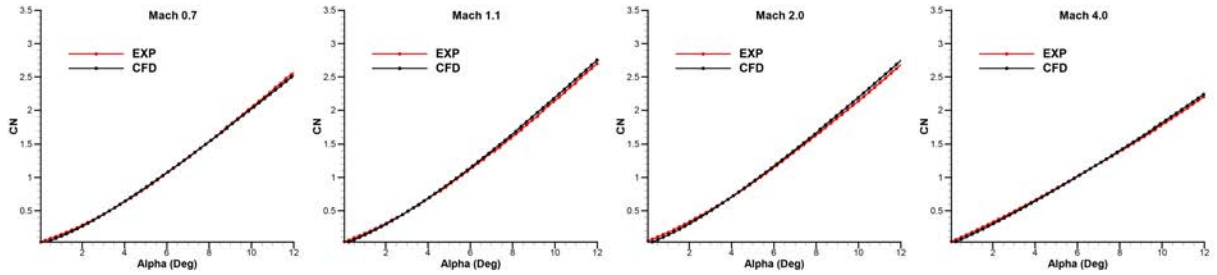

Fig. 6 Comparison of normal force coefficient obtained using CFD and experimental measurements, $\phi = 0°$.

Figure 7 is showing the variation of CN with roll angle with the model at 12° angle of attack. Much like the variation with pitch, the overall behavior of CN with roll angle is comparable, although the matching is not quite as close. Mach 0.7 and Mach 1.1 are showing better agreement than the supersonic Mach numbers shown. However, even at supersonic speeds, the change in roll angle dependence is captured well, providing more confidence that the CFD is producing the same general flow-fields that are observed in the experimental results. Therefore, additional information about the high-compressibility effects occurring above Mach 2 can be drawn from CFD with some confidence.

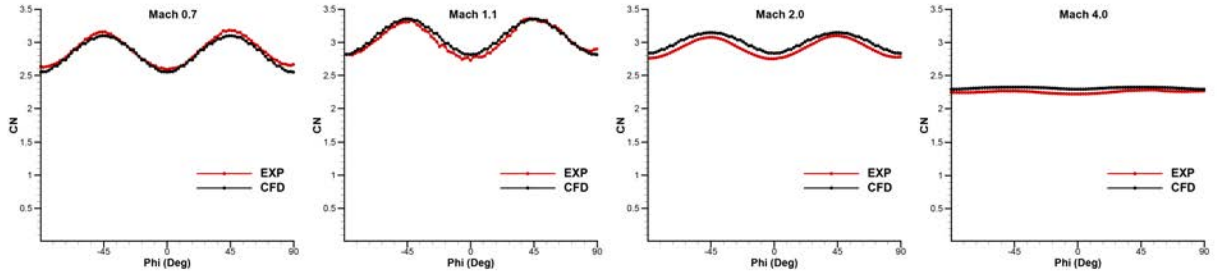

Fig. 7 Comparison of normal force coefficient obtained using CFD and experimental measurements, $\alpha = 12°$.

B. Drag Characteristics

The coefficient of drag characteristics included here are once again for the baseline, fixed-fin configuration. The results for the variation of CD with alpha are in figure 8 and are showing a typical non-linear increase. This is because, as alpha increases, the contribution of normal force becomes significant. At subsonic conditions, CD is lower at Mach 0.5 than at Mach 0.4 for all angles of attack tested. The unsteadiness at these Mach numbers is due to the base pressure correction term, which shows a larger influence at low speeds where static pressure is very high. For transonic conditions, CD_0 decreases with an increase in Mach number as well, both above and below Mach 1.0. The significant jump between Mach 0.9 and 1.1 is expected with the introduction of a leading shock. The changes in CD from Mach 0.6 to Mach 0.9, and from Mach 1.1 to Mach 1.2 become near negligible as the model is pitched. Supersonic variation in drag is showing to be significant. The reduction in CD_0 from Mach 2 to Mach 3 is much larger than that from Mach 3 to Mach 4. At $\alpha = 12°$, this difference is reduced due to the smaller difference in CN between Mach 2 and 3.

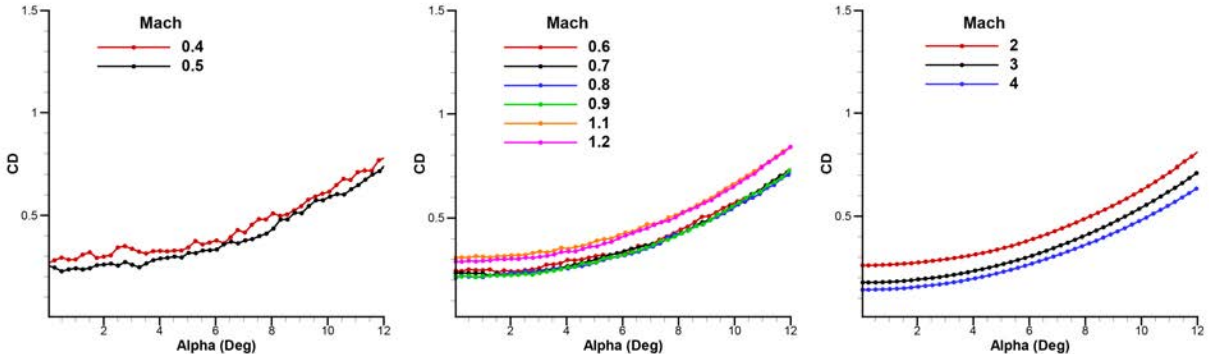

Fig. 8 Variation of drag coefficient with alpha at subsonic, transonic, and supersonic speeds, $\phi = 0°$.

C. Flow Visualization

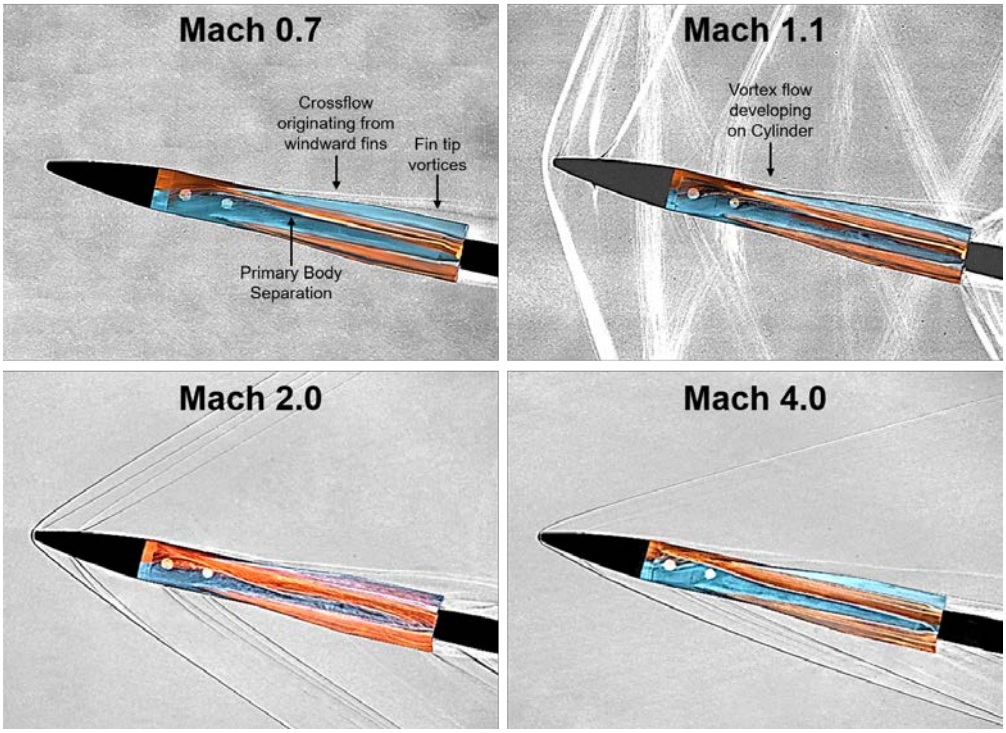

Fig. 9 Processed shadowgraph images with additional oil flow overlayed to highlight surface flow features, taken at $12°$ angle of attack and $0°$ of roll.

As noted in section III, high-speed shadowgraph video was taken along with all force and moment measurements and surface oil flow visualization runs were conducted to identify surface flow features. Figure 9 shows oil flow images overlayed on processed shadowgraph images to visualize how the surface flow features and surrounding flow-field develop. Results for Mach 0.7, 1.1, 2, and 4 are shown with the model in the 'x' configuration (ϕ=0°) and at α=12°. No shocks were visible on the model at Mach 0.7, but at Mach 1.1, the highly unsteady leading shock, as well as additional body shocks are highlighted by the rms image processing. At Mach 0.7, the fin tip vortices originating on the leeward fins are very well defined. However, with an increase in Mach number, these vortices appear to breakdown and are no longer visible at Mach 4. Directly above the leeward fin tip vortices, crossflow that appears to originate from the windward fins is clearly visible at all Mach numbers shown. Additionally, with an increase in Mach number, there is a

growth of vortex flow developing on the top of the cylinder. These features lead to this highly complex flow-field that will require additional advanced experimental techniques and high-fidelity CFD to fully resolve.

Oil flow images captured from the high-resolution video at Mach 2, α=12°, and ϕ = 0° are shown close up in Figure 10. Following the run, the model was rotated 360 degrees to capture the features on the entirety of model's surface. A top view, side view, and 45° middle view between them is shown. The development of the leeward fin tip vortices is very clear from the surface features in the top and 45° middle view. Development on the top of the windward fins is well defined in post test imaging as well. Additionally, shock-boundary layer interaction on the fin tips can be observed. How this fin SBLI interacts with the shear layer and flow along the top of the model will also be a future point of study. The oil flow features will also be used with additional experimental techniques to further study the complex flow-field that develops and the various interactions on the model. These results will also be compared to those derived from the CFD simulations to bolster confidence in other derived quantities that cannot be captured experimentally.

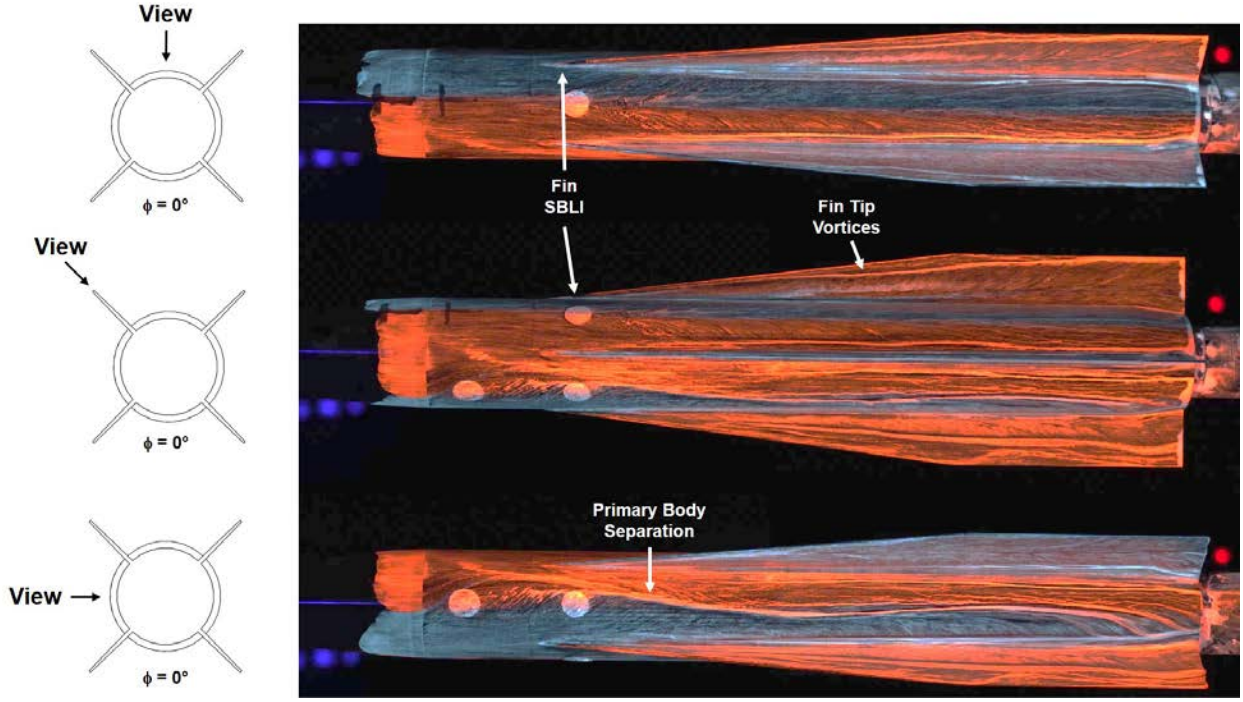

Fig. 10 Surface oil flow visualization taken at Mach 2 and 12° angle of attack.

D. Control Surface Effectiveness

With the testing of the second model, which utilized deflected control surfaces hinged at the midchord, the control surface effectiveness was determined. Control surface deflection cases were conducted at Mach 0.7 and Mach 2 in positive and negative elevator and aileron roll configurations. Magnitudes of deflection included 5°, 10°, and 20°. This model with deflection capabilities was also fitted with 0° surfaces. The coefficients of pitching moment and rolling moments were examined throughout 12° pitch sweeps at ϕ=0°. CRM was also examined during a 180° roll at α=12°. These results are shown in figures 11, 12, and 13. As shown in all three figures, control surface effectiveness for both pitching and rolling is clearly higher at Mach 0.7 than at Mach 2. Looking directly at the pitching behavior shown in figure 11, the CPM curves at Mach 0.7 and Mach 2 are very similar up to approximately 8° of pitch where at Mach 2, the slope levels off instead of staying negative. At both Mach numbers, the baseline CPM curve is generally mirrored with fin deflection in all cases, with the exception of the 20°, positive elevator case at Mach 0.7. Overall effectiveness increases with an increase in deflection as the magnitude of change in CPM with 10° deflection is more than two times the magnitude of change in CPM with 5° deflection. This also holds true for 20° deflection as the magnitude of change more than doubles that of 10° deflection, once again with the exception of the positive elevator case at Mach 0.7.

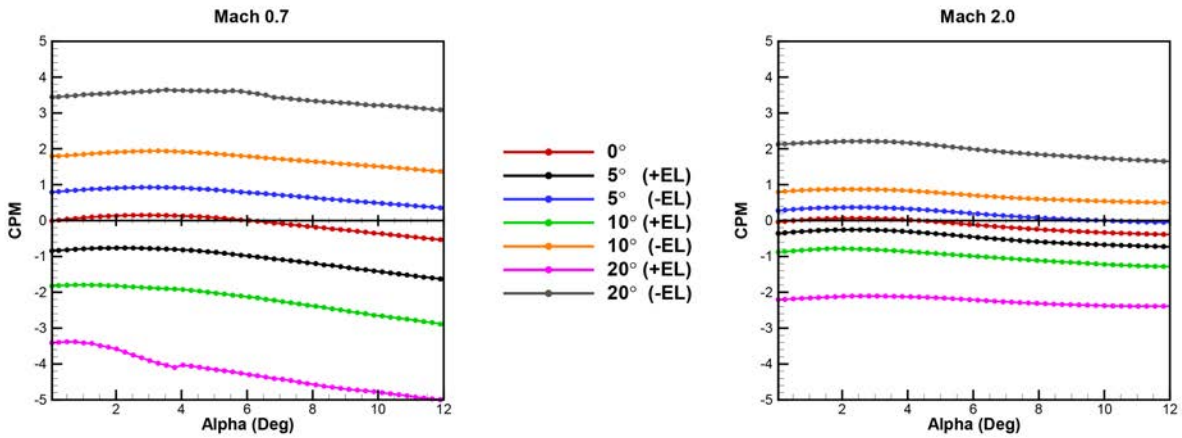

Fig. 11 Coefficient of pitching moment versus alpha at 0° of roll, produced by positive and negative elevator configurations.

Considering roll effectiveness in figure 12, aside from the overall increase in effectiveness at Mach 0.7 compared to Mach 2, the CRM versus alpha curves are similar at both Mach numbers for 5° and 10° cases. However, with 20° deflection at Mach 2, the CRM is decreasing with increased alpha whereas at Mach 0.7, the CRM continues the trend of having a very minor increase with alpha. To determine the exact flow mechanism causing this reduced effectiveness at Mach 2, the compressibility effects on the shear layer need to be explored further.

Overall control surface roll effectiveness, similar to pitch effectiveness, does increase with an increase in deflection angle. The average CRM at 10° is more than two times that at 5°, and the average CRM at 20° is more than two times that at 10°.

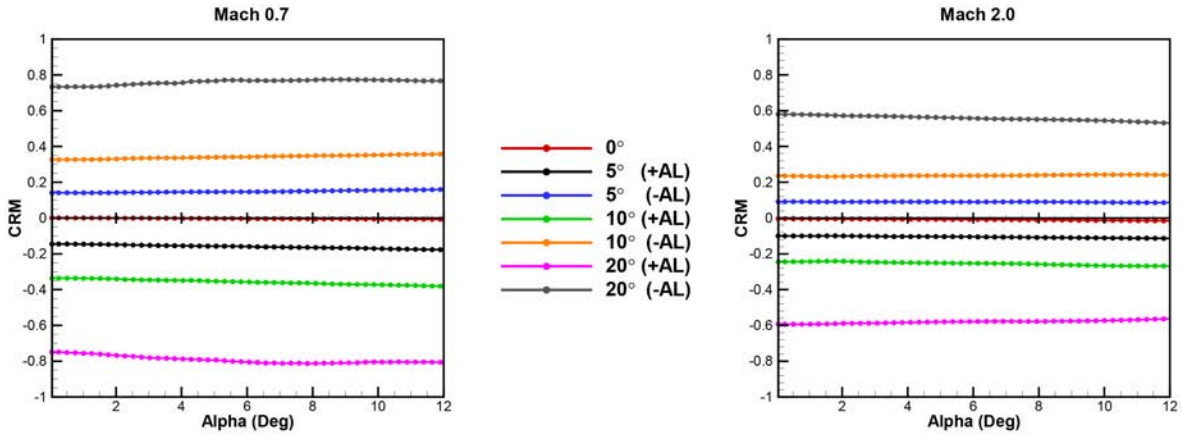

Fig. 12 Coefficient of rolling moment versus alpha at 0° of roll, produced by positive and negative aileron roll configurations.

Due to the significant roll dependence of CN, indicating vortex-fin interactions and likely a variance in the shear layer flow-field structure, the effect of roll angle on control surface roll effectiveness is shown in figure 13. Here, CRM is plotted against phi with the model pitched at $\alpha = 12°$. At Mach 0.7, roll effectiveness is shown to depend on roll angle at all magnitudes of deflection, showing a sinusoidal relationship with a 90° period. The peaks and troughs of this behavior is reached at increments of 22.5°, between the 'x' and the '+' configurations. At Mach 2 however, this dependence isn't observed. Small variations do occur, but the true pattern of behavior at Mach 2 is difficult to discern. The flow mechanisms causing the roll dependence appear to be mitigated by the compressibility effects at Mach 2. More detailed flow diagnostics will be needed to study the flow-field that occurs at Mach 0.7 to gain an understanding of this disparity.

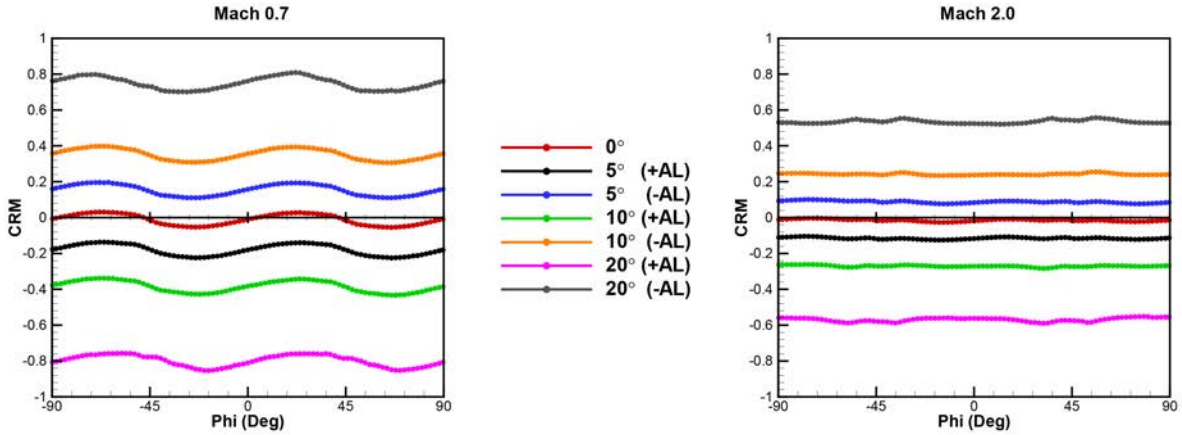

Fig. 13 Coefficient of rolling moment versus phi at 12° angle of attack, produced by positive and negative aileron roll configurations.

IV. Aerodynamic Modeling for Flight Dynamics and Control

A. Introduction

The first set of tests that was used in the experimental determination of the aerodynamic coefficients of the vehicle was a test in which the model was pitched up from 0 to 12 degrees angle of attack (α). The tests were conducted over a sweep of Mach numbers. At each Mach number two tests were conducted one in which the projectile was rolled to 0 degrees, and one in which the projectile was rolled to 45 degrees.

With a pitching case only the axial force, pitching moment, and normal force can be used to predict the aerodynamic coefficients. With the test being quasi-steady a simplified aero model can be constructed. The model is shown in eqs. (6) and (7).

$$\begin{Bmatrix} X \\ Z \end{Bmatrix} = -\frac{\pi}{8} V^2 D^2 \rho \begin{Bmatrix} C_X \\ C_{\mathrm{NA}} \frac{w}{V} \end{Bmatrix} \tag{6}$$

$$M = \frac{\pi}{8} V^2 D^3 \rho C_{\mathrm{MA}} \frac{w}{V} \tag{7}$$

Where the coefficients are determined using the following augmented polynomial expressions.

$$C_X = C_{X0} + C_{X2}\alpha^2 + 2C_{X\gamma}\alpha \cos(4\phi) \tag{8}$$

$$C_{\mathrm{NA}} = C_{\mathrm{NA0}} + C_{\mathrm{NA2}}\alpha^2 + C_{\mathrm{NA4}}\alpha^4 + 2C_{\mathrm{NA}\gamma}\alpha \cos(4\phi) \tag{9}$$

$$C_{\mathrm{MA}} = C_{\mathrm{MA0}} + C_{\mathrm{MA2}}\alpha^2 + C_{\mathrm{MA4}}\alpha^4 + 2C_{\mathrm{MA}\gamma}\alpha \cos(4\phi) \tag{10}$$

A least squares regression is then performed to determine the optimal values of $C_{X0}, C_{X2}, C_{X\gamma}, C_{\mathrm{NA0}}, C_{\mathrm{NA2}}, C_{\mathrm{NA4}}, C_{\mathrm{NA}\gamma}, C_{\mathrm{MA0}}, C_{\mathrm{MA2}}, C_{\mathrm{MA4}}$, and $C_{\mathrm{MA}\gamma}$.

B. Least Squares Regression Method Comparison

Two methods were investigated in the implementation of the least squares regression. The first method is a least squares regression between the measured forces and moments and the forces and moments computed using eqs. (6) and (7). The second method is where the measured forces and moments are used to compute the experimental value of the coefficients by rearranging eqs. (6) and (7) to solve for the coefficients rather than the forces and moments. Like the first method the computed coefficients are still determined with eqs. (8) to (10) and the regression is performed using the experimental and computed coefficients.

A significant issue with the second method is that to compute C_{NA} and C_{MA} $\frac{V}{w}$ needs to be computed and at small angles of attack w is close to zero which means $\frac{V}{w}$ will be very large. This means that the coefficients can not be accurately computed for low angles of attacks. Thus the second method does not take into account the behaviour of the projectile at low α.

A comparison of the two methods is presented below for the Mach 2.0 test cases.

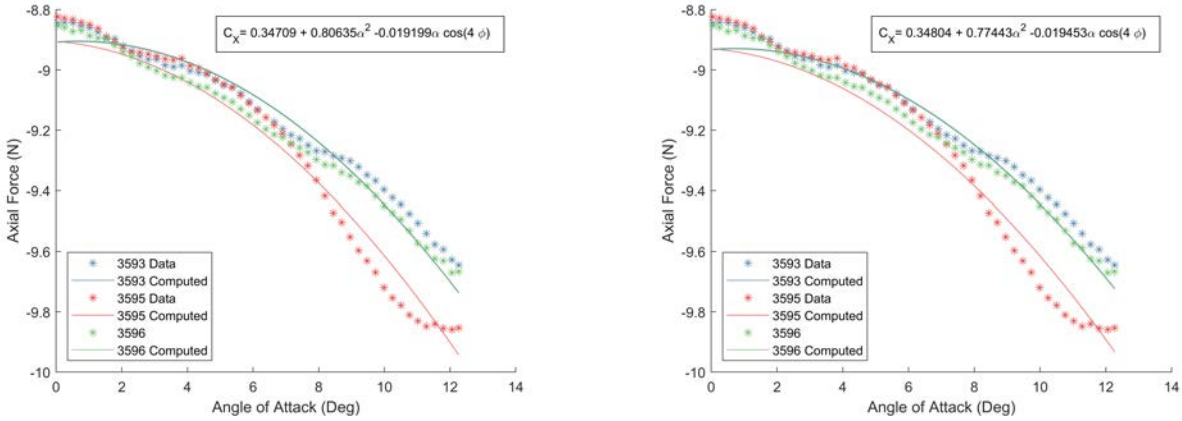

(a) Measured Axial force **(b) C_X computed from pitching moment.**

Fig. 14 Plots of the measured pitching moment and computed pitching moment. The pitching moment was computed using a least squares regression with the measured moment fig. 14a and a regression using C_X which was computed using the measured moment fig. 14b.

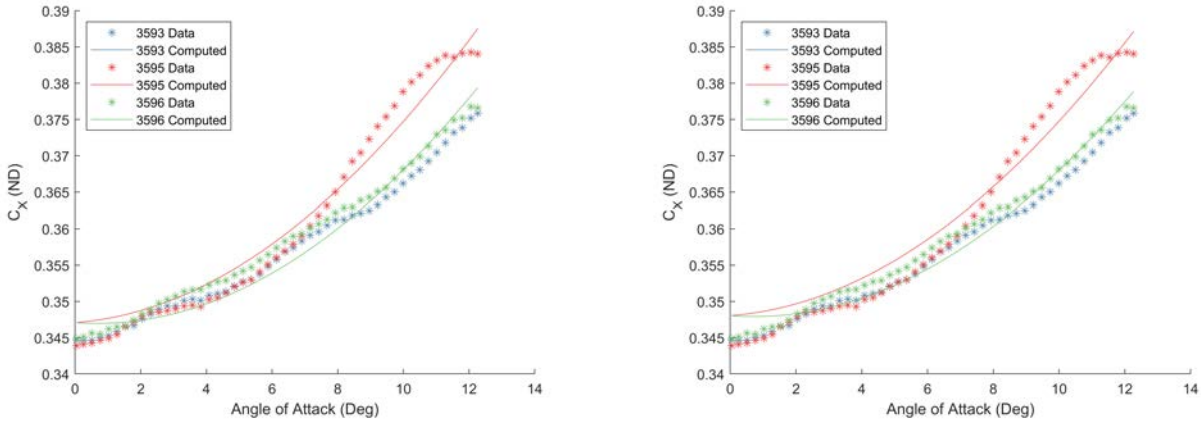

(a) Measured pitching moment **(b) C_{Ma} computed from pitching moment.**

Fig. 15 Plots of C_X computed from the measured moment, and from the regression analysis. The regression was performed with the measured moment fig. 15a and a regression using C_X which was computed using the measured moment fig. 15b.

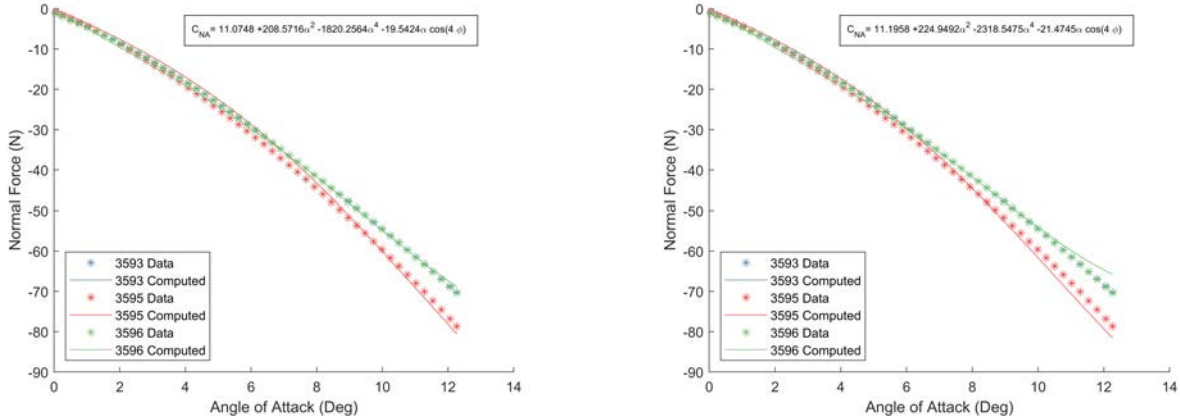

(a) Measured Normal force **(b) C_{NA} computed from normal force.**

Fig. 16 Plots of the normal force and computed normal force. The normal force was computed using a least squares regression with the measured force fig. 16a and a regression using C_{NA} which was computed using the measured force fig. 16b.

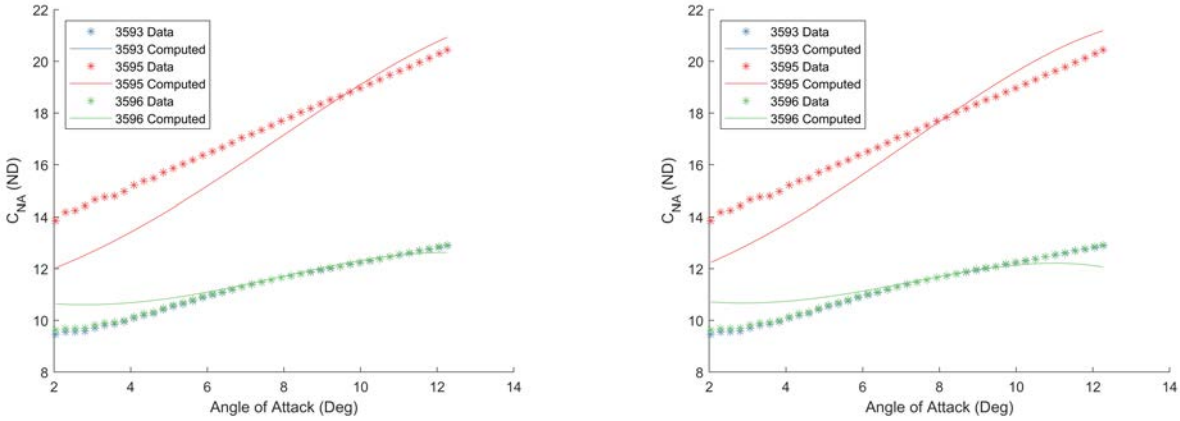

(a) Measured normal force **(b) C_{NA} computed from normal force.**

Fig. 17 Plots of C_{NA} computed from the measured normal force, and from the regression analysis. The regression was performed with the measured force fig. 17a and a regression using C_{NA} which was computed using the measured force fig. 17b.

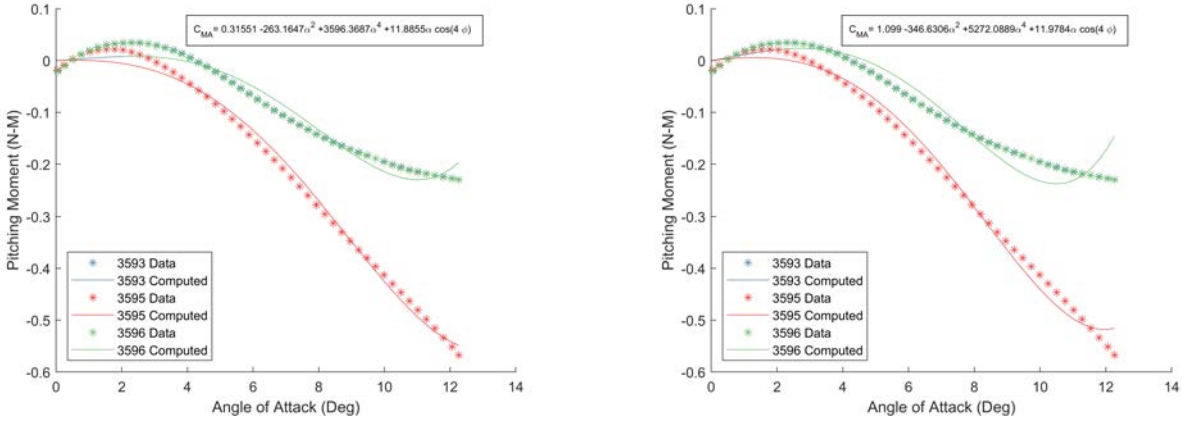

(a) Measured pitching moment **(b) C_{Ma} computed from pitching moment.**

Fig. 18 Plots of the measured pitching moment and computed pitching moment. The pitching moment was computed using a least squares regression with the measured moment fig. 18a and a regression using C_{Ma} which was computed using the measured moment fig. 18b.

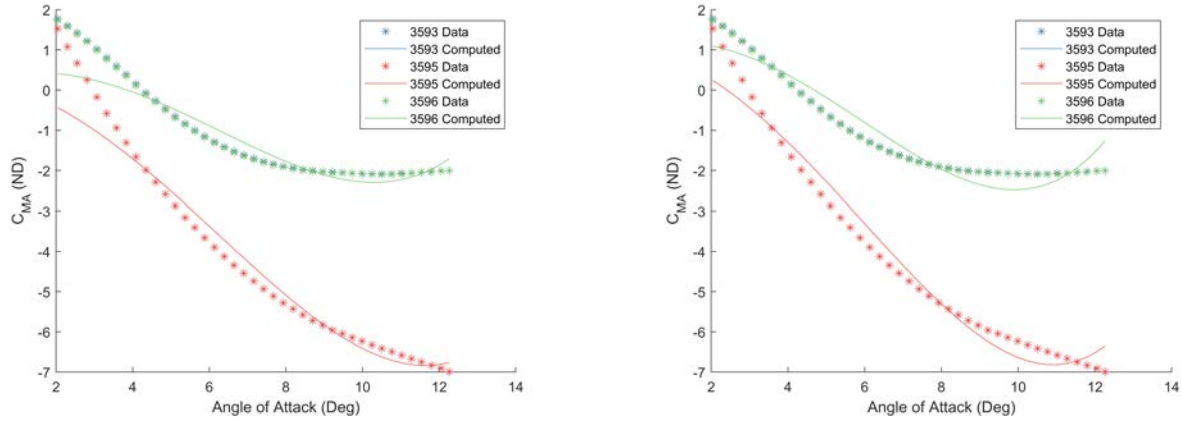

(a) Measured pitching moment **(b) C_{Ma} computed from pitching moment.**

Fig. 19 Plots of C_{MA} computed from the measured moment, and from the regression analysis. The regression was performed with the measured moment fig. 19a and a regression using C_{Ma} which was computed using the measured moment fig. 19b.

Table 1 Comparison of R^2 values for regression performed with the forces and moments and regression using the coefficients.

Coefficient	force Regression R^2 force	coefficient Regression R^2 force	Force Regression R^2 Coefficient	Coefficient Regression R^2 Coefficient
C_X	0.9664	0.9638	0.9593	0.9631
C_{NA}	0.9974	0.9937	0.9496	0.9553
C_{MA}	0.9876	0.9744	0.9644	0.9760

When looking at the data it was decided to use the first method for the rest of the study due to the fact that the method can be used at low α. Projectiles commonly fly at low α and so using a method that is viable at low α is an important factor.

C. Mach Comparison

The coefficients were then computed for all of the different Mach numbers at which tests were conducted.

The plots of the variation in the axial force coefficients are shown in fig. 20. The plot of the coefficient of determination for the cases are shown in fig. 21. One of the most interesting results is that the R^2 value in the transonic regime decreases drastically and even becomes less than 0. This means that the model that has been used to model C_X needs to be modified to provide an accurate representation of the projectile in the transonic regime.

Another interesting trend that is present in the data is that the effect of changes in the roll angle of the projectile decreases with an increase in flow speed. This is evident in both C_{NA} and C_{MA} but for C_X there appears to be no correlation with the effect of the roll angle and flight speed.

Another interesting observations in the data for C_{MA} is that there is a sharp drop in the R^2 value at Mach 4.8. This likely can be attributed to the fact that at this speed the wind tunnel could not maintain a constant speed and throughout the trial there was a noticeable drop in the velocity of the tunnel. This is significant because due to differences in data acquisition the tunnel velocity measurements could not be directly correlated to the measurement of the force and moments and thus the the instantaneous velocity measurements were averaged. The average velocity was assumed to be the tunnel velocity for all of the test points. As can be seen in fig. 26 there is a significant increase in the deviation of the velocity from the mean at Mach 4.8.

Table 2 Variation of C_{NA} coefficients with Mach.

Mach	C_{NA0}	C_{NA2}	C_{NA4}	$C_{\mathrm{NA}\gamma}$	R^2 Normal Force	R^2 C_{NA}
0.4	9.430	311.383	-3280.434	-11.873	0.9978	0.9771
0.5	10.048	277.693	-2725.760	-12.121	0.9966	0.9575
0.6	10.127	260.882	-2581.623	-11.458	0.9975	0.9640
0.7	9.874	268.900	-2569.329	-11.207	0.9980	0.9675
0.8	10.009	273.156	-2774.564	-11.337	0.9975	0.9652
0.9	9.908	279.490	-2814.996	-11.219	0.9980	0.9715
1.1	10.620	261.213	-2343.205	-11.487	0.9980	0.9686
1.2	11.365	252.257	-2347.367	-11.933	0.9974	0.9610
2.0	11.075	208.572	-1820.256	-9.771	0.9974	0.9496
3.0	11.407	125.619	-1014.520	-8.119	0.9968	0.9353
4.0	10.813	66.803	-373.485	-6.607	0.9946	0.8864
4.8	7.283	77.955	-611.975	-4.476	0.9955	0.8879

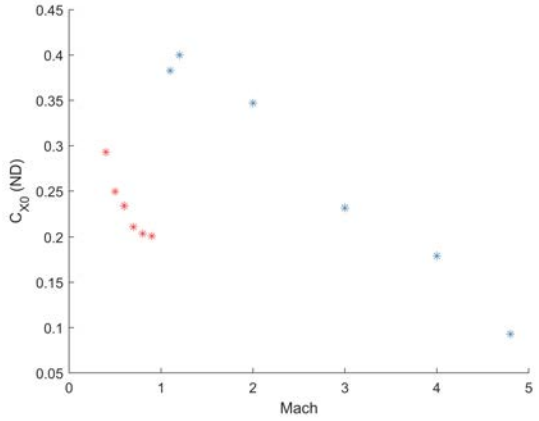

(a) C_{X0}

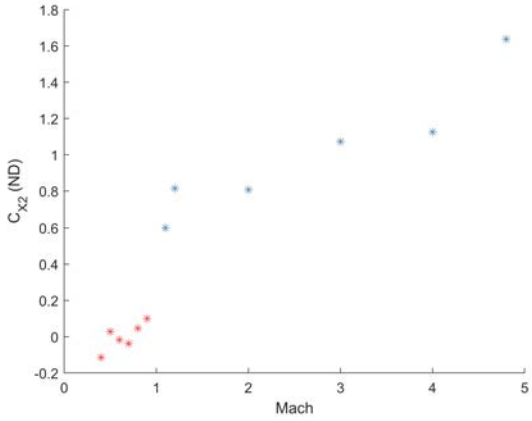

(b) C_{X2}

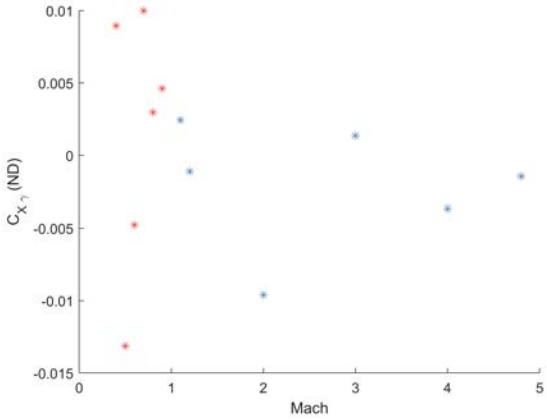

(c) $C_{X\gamma}$

Fig. 20 Variation of the axial force coefficient with Mach number.

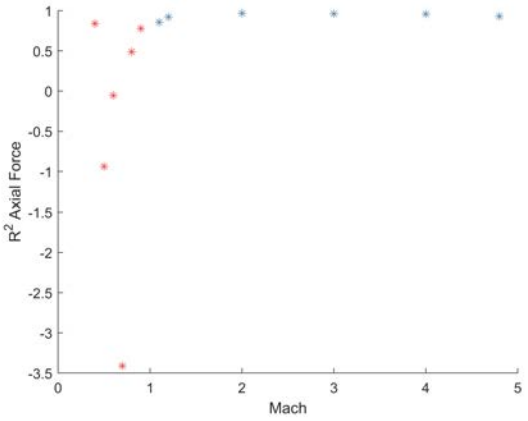

(a) R^2 **of the axial force**

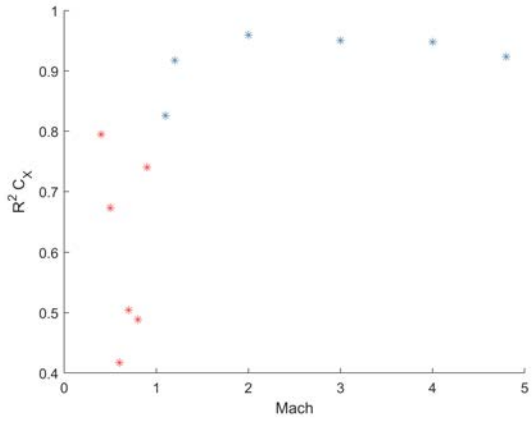

(b) R^2 **of the** C_X **coefficient.**

Fig. 21 R^2 **of the axial force and coefficient.**

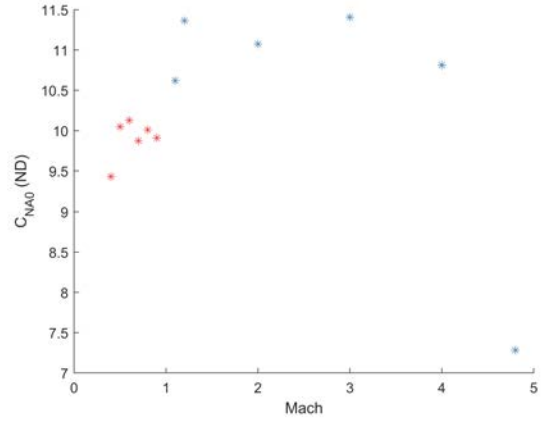

(a) $C_{\mathbf{NA}0}$

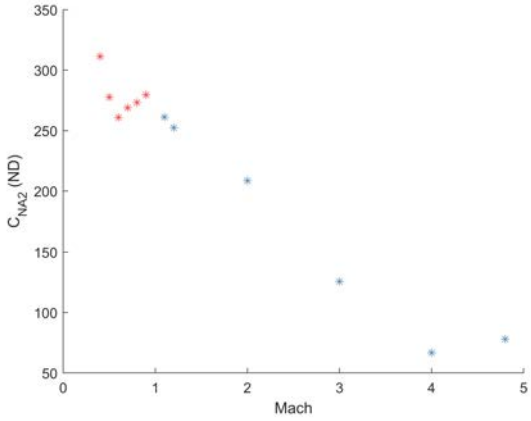

(b) $C_{\mathbf{NA}2}$

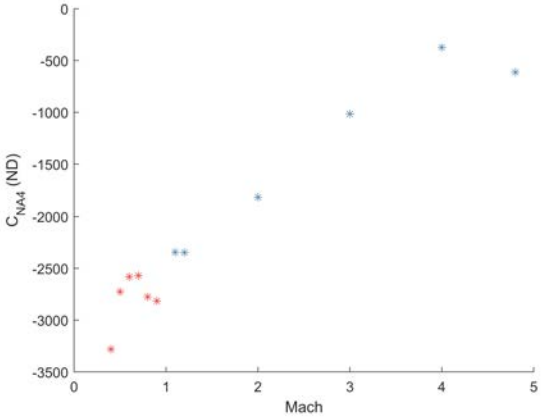

(c) $C_{\mathbf{NA}4}$

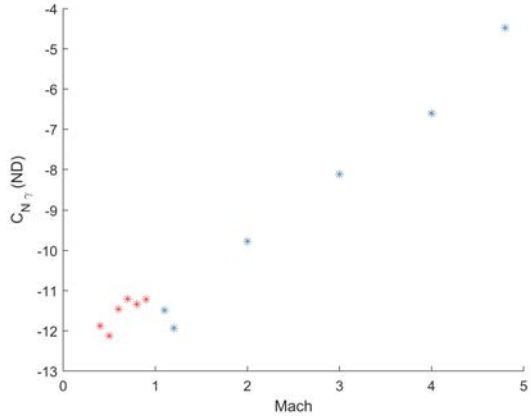

(d) $C_{\mathbf{NA}\gamma}$

Fig. 22 Variation of the normal force coefficient with Mach number.

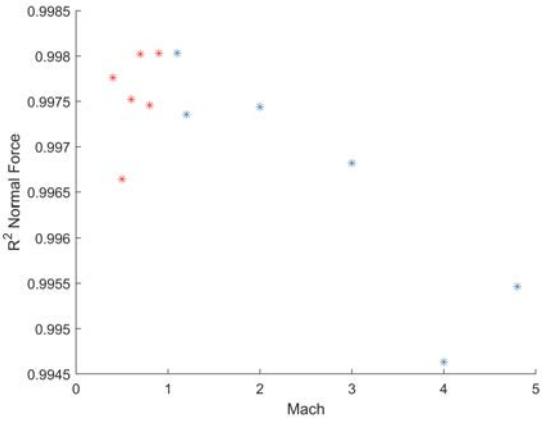

(a) R^2 **normal force**

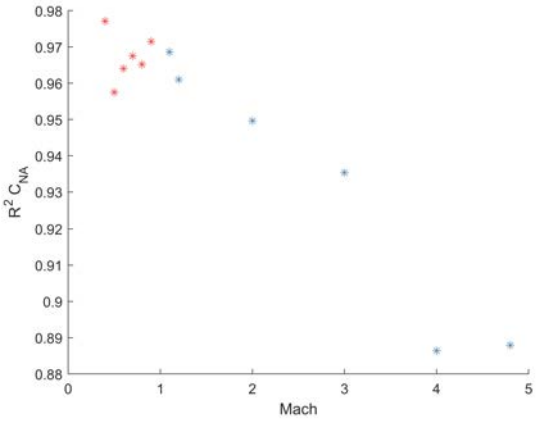

(b) R^2 **normal force coefficient**

Fig. 23 R^2 **of the normal force and coefficient.**

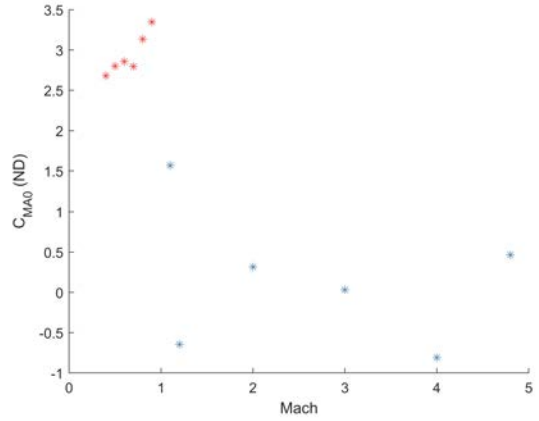

(a) $C_{\mathbf{MA}0}$

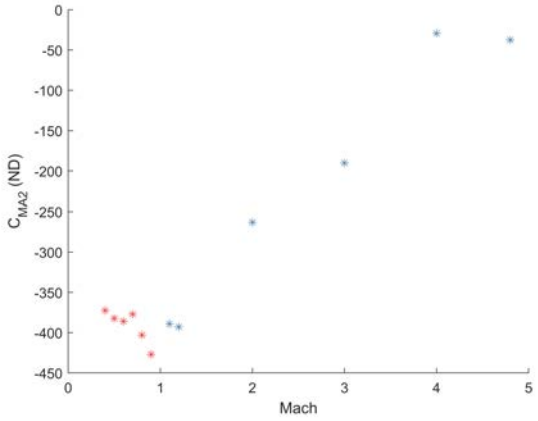

(b) $C_{\mathbf{MA}2}$

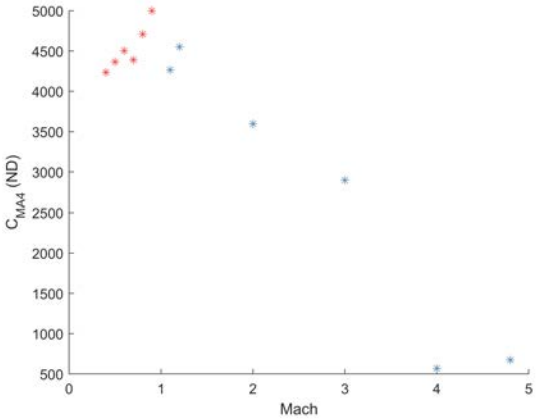

(c) $C_{\mathbf{MA}4}$

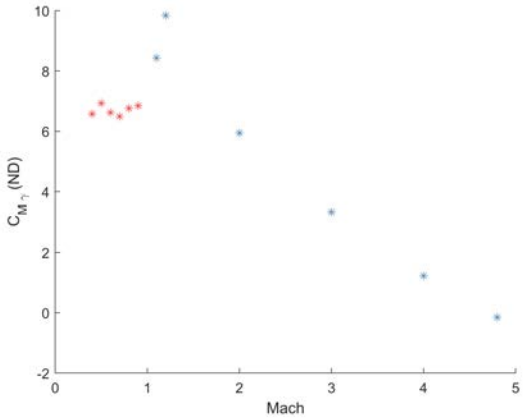

(d) $C_{\mathbf{MA}\gamma}$

Fig. 24 Variation of the pitching moment coefficient with Mach number.

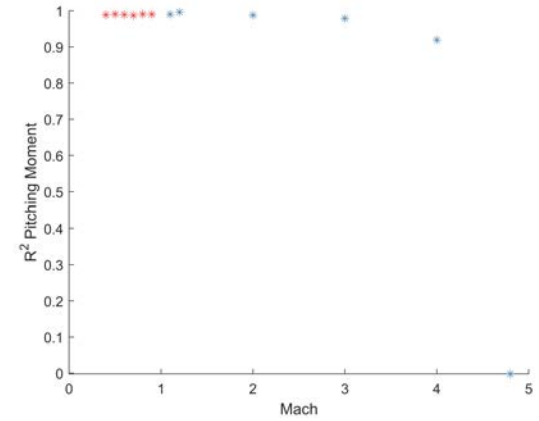

(a) R^2 **pitching moment**

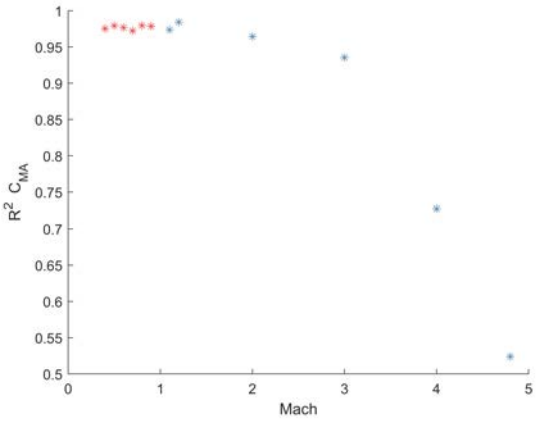

(b) R^2 **pitching moment coefficient**

Fig. 25 R^2 **of the pitching moment and coefficient.**

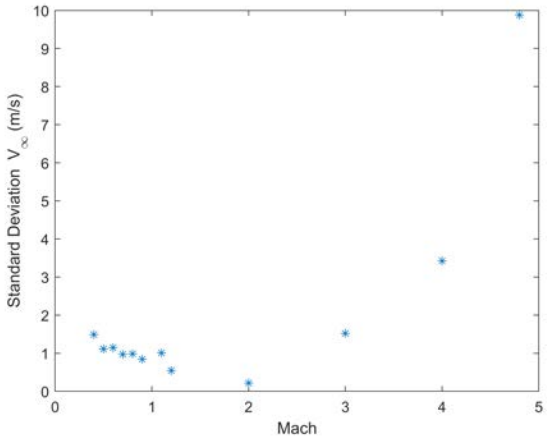

Fig. 26 Wind tunnel velocity variation.

Table 3 Variation of C_{MA} coefficients with Mach.

Mach	C_{MA0}	C_{MA2}	C_{MA4}	$C_{MA\gamma}$	R^2 Pitching Moment	R^2 C_{MA}
0.4	2.681	-372.484	4235.275	6.573	0.9884	0.9753
0.5	2.800	-382.458	4366.204	6.931	0.9904	0.9794
0.6	2.857	-385.978	4502.217	6.618	0.9888	0.9767
0.7	2.796	-377.206	4389.331	6.492	0.9873	0.9723
0.8	3.135	-403.046	4708.694	6.759	0.9903	0.9795
0.9	3.347	-427.051	4999.314	6.843	0.9901	0.9785
1.1	1.567	-389.019	4265.130	8.431	0.9900	0.9738
1.2	-0.645	-392.965	4549.858	9.837	0.9961	0.9842
2.0	0.316	-263.165	3596.369	5.943	0.9876	0.9644
3.0	0.033	-190.308	2896.649	3.336	0.9786	0.9354
4.0	-0.810	-29.377	568.421	1.221	0.9193	0.7275
4.8	0.466	-37.622	673.077	-0.153	-0.0021	0.524

Table 4 Variation of C_X coefficients with Mach.

Mach	C_{X0}	C_{X2}	$C_{X\gamma}$	R^2 Axial Force	R^2 C_X
0.4	0.2931	-0.1143	0.008957	0.8385	0.7949
0.5	0.2494	0.0282	-0.013141	-0.9393	0.6737
0.6	0.2339	-0.0174	-0.004772	-0.0544	0.4171
0.7	0.2112	-0.0377	0.009994	-3.4097	0.5045
0.8	0.2036	0.0460	0.002975	0.4872	0.4889
0.9	0.2010	0.0992	0.004616	0.7779	0.7400
1.1	0.3828	0.6001	0.002437	0.8556	0.8261
1.2	0.4000	0.8143	-0.001111	0.9218	0.9173
2.0	0.3471	0.8063	-0.009599	0.9664	0.9593
3.0	0.2318	1.0732	0.001354	0.9604	0.9506
4.0	0.1791	1.1253	-0.003652	0.9574	0.9479
4.8	0.0928	1.6378	-0.001446	0.9293	0.9234

V. Conclusions

The main objectives of this experimental study were to generate aerodynamic data for the validation of a numerical tool and evaluate the control surface effectiveness over a range of flow conditions. The CFD generated normal force coefficients showed quality agreement with experimental results across multiple Mach numbers and produced the same roll dependant behavior. Experimental results showed a significant variation in CN at higher angles of attack ($\alpha > 8°$) for Mach numbers greater than Mach 2, as well as a significant reduction in roll orientation dependence. Significant variation between supersonic and transonic behavior was also observed when looking at control surface effectiveness. Overall, control surface effectiveness was notably reduced from Mach 0.7 to Mach 2, as well as changes in behavior with alpha were observed for both CPM and CRM. These observations, in conjunction with flow visualization indicate there are significant compressibility effects on the shear layer produced by this configuration. While this would generally be expected, it is of interest to conduct a more detailed study into the underlying flow physics that cause these effects. The data collected here will be used as a basis for future study with more advanced flow diagnostic techniques in the FSU PSWT to fully resolve and characterize the flow-fields generated by this configuration across an extended Mach regime.

Acknowledgments

The authors would like to acknowledge the U.S. Army Research Office for their financial support under cooperative agreement W911NF2020076 managed by Dr. Matthew Munson. The authors would like to thank Dr. Jonas Gustavsson, Mr. Alex Karns and Mr. Jeremy Phillips for their support during wind tunnel testing.

References

[1] Mayo, E. E., *Newtonian aerodynamics for tangent ogive bodies of revolution*, Vol. 3337, National Aeronautics and Space Administration, 1966.

[2] Dolling, D., and Bogdonoff, S., "Supersonic, High Reynolds Number Flow Over a Tangent Ogive Cylinder at Small Angles of Attack. An Experimental Study and Comparison with Theory," Tech. rep., Princeton Univ Nj Dept Of Mechanical And Aerospace Engineering, 1979.

[3] Faro, I. D., and Faro, D., "Handbook of supersonic aerodynamics. Section 8. Bodies of revolution," Tech. rep., Johns Hopkins Univ Laurel Md Applied Physics Lab, 1961.

[4] Kellock, R. E., and Miller, P. H., "Aerodynamic Characteristics of Basic Nose-Cylinder Bodies for Large Ranges of Angle of Attack," Tech. rep., Air Force Armament Lab Eglin AFB FL, 1971.

[5] Dennis, D. H., and Cunningham, B. E., "Forces and Moments on Pointed and Blunt-nosed Bodies of Revolution at Mach Numbers from 2.75 to 5.00," Tech. rep., NACA, 1952.

[6] Dennis, D. H., and Cunningham, B. E., "Forces and moments on inclined bodies at Mach numbers from 3.0 to 6.3," 1954.

[7] Allen, H. J., and Perkins, E. W., *Characteristics of flow over inclined bodies of revolution*, National Advisory Committee for Aeronautics, 1951.

[8] Jorgensen, L. H., and Perkins, E. W., "Investigation of some wake vortex characteristics of an inclined ogive-cylinder body at Mach number 2," 1958.

[9] Paul, B. P., and Wedemeyer, E., "An Investigation of the Flow About an Ogive Cylinder at High Angles of Incidence," Tech. rep., Von Karman Inst For Fluid Dynamics Rhode-Saint-Genese (Belgium), 1982.

[10] Oberkampf, W. L., and Bartel, T. J., "Symmetric body vortex wake characteristics in supersonic flow," *AIAA Journal*, Vol. 18, No. 11, 1980, pp. 1289–1297.

[11] Mello, J. F., "Investigation of normal force distributions and wake vortex characteristics of bodies of revolution at supersonic speeds," *Journal of the Aerospace Sciences*, Vol. 26, No. 3, 1959, pp. 155–168.

[12] Dawson, D., Kumar, R., Kirby, S., Birch, T. J., and Taylor, R., "Experimental and Numerical Analysis of Fin Effectiveness on an Axisymmetric Configuration," *2018 AIAA Aerospace Sciences Meeting*, 2018, p. 1524.

[13] Dawson, D., Kumar, R., Parker, L., Kirby, S., Birch, T. J., and Taylor, R., "Aerodynamic characterization of an axisymmetric body with fins at supersonic speeds," *2018 AIAA Aerospace Sciences Meeting*, 2018, p. 1523.

[14] Dawson, D. P., "Aerodynamic Characteristics of an Ogive Cylinder Body with Fins," 2019.

[15] Pokela, R. C., Foster, D., Munroe, M., Koos, J., Mason, F., Kumar, R., McPherson, B., and Taylor, R. H., "Experimental Study of Axisymmetric Projectile Configurations at Supersonic Speeds," *AIAA Scitech 2021 Forum*, 2021, p. 0135.

[16] Nielsen, J., "Nonlinearities in missile aerodynamics," *16th Aerospace Sciences Meeting*, 1978, p. 20.

[17] Vasile, J. D., and Sahu, J., "Roll OrientationDependent Aerodynamics of a Long-Range Projectile," Tech. rep., CCDC Army Research Laboratory Aberdeen Proving Ground United States, 2020.

[18] Vasile, J. D., Bryson, J., and Fresconi, F., "Aerodynamic Design Optimization of Long Range Projectiles using Missile DATCOM," *AIAA Scitech 2020 Forum*, 2020, p. 1762.

[19] Vasile, J. D., Bryson, J. T., Sahu, J., Paul, J. L., and Gruenwald, B. C., "Aerodynamic Dataset Generation of a Long-Range Projectile," Tech. rep., CCDC Army Research Laboratory Aberdeen Proving Ground United States, 2020.